Application of the 3D time-domain Green's function for finite water depth in hydroelastic mechanics

Peng Yang [a], Jingru Li [a,*], Xuekang Gu [b], Dongwei Wu [c]

[a] Department of Mechanics and Electrics Engineering, Hainan University, No. 58 Renmin Road, Meilan District, Haikou, 570228, China
[b] China Ship Scientific Research Center, No. 222 East Shanshui Road, Binhu District, Wuxi, 214082, China
[c] China Ship Development and Design Center, No. 268 Zhangzhidong Road, Wuchang District, Wuhan, 430064, China

ABSTRACT

Based on the boundary element method and the superposition principle of structural elastic modes, the three-dimensional time-domain Green's function in finite water depth is applied to hydroelasticity, and the theoretical basis of three-dimensional time-domain hydroelasticity is established. To address the difficulty and divergence of the three-dimensional time-domain Green's function in finite water depth, a numerical solution method that has high accuracy and good stability is developed using series expansion, asymptotic methods and fourth-order differential equations. Taking a large bulk carrier as an example, the corresponding predictions of resonance frequency, motion, wave load and hydroelastic response with speed in finite water depth are carried out. The numerical results are compared with the results of the three-dimensional frequency domain method and the time-domain method of inner and outer region matching and are verified by the towing model test. The three-dimensional time-domain hydroelastic theory and numerical method established in this paper are of great significance for fluid coupling analysis, structural dynamic response research and wave load prediction of complex floating bodies with speed.

1. Introduction

The basic mathematical model of three-dimensional hydroelasticity was first developed by Wu (1984). Furthermore, the hydroelastic problems with forward speed have been studied in the frequency domain (Du, 1996) and the time domain (Wang, 1996) for infinite water depth. The Green's function with forward speed in the frequency domain has been directly utilized (Du, 1996), and the Green's function with forward speed in the time domain has also been utilized (Wang, 1996). The theory of 3D second-order nonlinear hydroelasticity in the frequency domain has been presented (Wu et al., 1997). The second-order hydroelastic responses of a VLFS have been investigated (Maeda et al., 1997; Ikoma et al., 1998). Furthermore, based on the second-order nonlinear hydroelastic theory, software has been developed and applied to the mooring analysis of a ship hull (Chen, 2001) and to the prediction of nonlinear hydroelastic responses of a SWATH in irregular waves (Tian and Wu, 2006). The inner and outer region matching method has been applied in the time domain (Liu et al., 2006; Liu and Papanikolaou, 2011) and in 3D hydroelasticity models (Yang, 2016). The Rankine source has been used in the inner region, and the

Green's function of infinite water depth has been used in the outer region.

In the past two decades, the scale of ships has increased rapidly. For example, the maximum volume of a container has increased from several thousand to more than 22,000 TEU. Because large ships are generally constructed of high-strength steel and because some of them have large openings, their hulls are relatively soft under wave loads. Their hydroelastic effects are obvious, so they are prone to vertical and torsional wave-induced vibration (called springing). The springing of an ultra-large ore carrier was investigated using the 3D second-order nonlinear hydroelastic method in the frequency domain (Hu et al., 2012). The wave load transfer functions and the hydroelastic responses of the carrier in irregular waves are given for the cases of zero speed and forward speed and for heading and oblique wave directions. At the same time, the results are compared with the data from model tests, and the influence of wave-induced vibration on structural fatigue is evaluated. Furthermore, the nonlinear hydroelastic responses, springing and whipping of a large bulk carrier in infinite water depth are studied by means of the inner and outer region matching method and model tests (Yang, 2016; Yang et al., 2018).

---

* Corresponding author.
  E-mail address: leslieljr@sina.com (J. Li).

On the other hand, due to the emergence of large offshore structures or multi-module floating structures, the hydroelastic method has been more widely used. These structures have large deflections and nonlinear responses, so a better method than the hydroelastic method to solve problems involving these structures, such as VLFSs and large flexural fish cages, is the time domain method. The fish cage group structure with hinged connectors has elastic torsion and vertical bending, as well as multiple rigid body modes (Fu and Moan, 2012). The dynamic responses between the modules of the cage group structure are mainly controlled by relative rigid body motion modes in heading waves. However, the elastic torsional mode contributes more to oblique waves than to heading waves, so it is necessary to consider the elastic deformation responses of the structure. From the viewpoint of analysing the dynamic responses of the water surface bracing frame, the net clothing and the mooring system attached to the fishery and aquaculture platform, only the damping effect needs to be considered. Furthermore, the nonlinear hydroelastic analysis of a single cage structure in irregular waves was carried out (Li et al., 2013). The authors concluded that there are large motions and deformations of the cage in waves. The effect of low-order modes on motion and structural stress is more important than that of high-order modes. On the other hand, the contribution of wave energy generation devices and auxiliary buoys in reducing the hydroelastic responses of very large floating structures has been studied (Nguyen et al., 2019), and the hydroelastic responses of legged floating box structures have also been studied by numerical methods and model tests (Wu et al., 2019). Some researchers have combined the Boussinesq equation with the Rankine source to form a direct coupling method in the time domain by considering wave evolution near the reef and the hydroelastic effect of the floating structures (Ding et al., 2017). The motions and dynamic responses of very large floating structures have been predicted, and the numerical results have been verified by model tests. Furthermore, the hydroelastic responses of one 8-module very large floating structure and the load principles of connectors have been analysed by considering the non-uniformity of wave parameters in time and space fields; in addition, model tests for verification have been carried out (Ding et al., 2019).

In recent years, the three-dimensional hydroelastic method has been more widely used. At the same time, increasingly complex problems need to be solved by the time-domain method. At present, in the framework of potential flow theory, there are two main types of three-dimensional hydroelasticity based on the time-domain method: (1) the boundary element and three-dimensional time-domain Green's function (Wang and Wu, 1996); and (2) the boundary element combined with the Rankine source (Yang, 2016). It can be seen from the above summary that there is little research involving 3D hydroelasticity in the time domain for finite water depth. In this paper, a three-dimensional hydroelastic method in the time domain is established based on the three-dimensional time-domain Green's function in finite water depth, and a solution method for the three-dimensional time-domain Green's function is given; the model test is carried out in the towing tank. The correctness of the theory and the numerical method is verified by cross-comparison among the numerical results and the experimental results.

2. Fundamental theory and mathematical formulation

2.1. Basic assumptions

When the interaction between floating structures and waves is studied, the fluid around the elastic ship hull is usually assumed to be uniform incompressible, non-viscous, and non-rotating; moreover, the effects of lift force and surface tension are not considered. On the other hand, it is assumed that the elastic deformation of the structure is small and that the overall response satisfies the linear superposition principle of modal deformation.

The translational displacement $\vec{u}$ and rotation $\vec{\theta}$ at any position of the ship structure may be expressed as an aggregate of the displacements of its principal modes (Wu, 1984; Price and Wu,1984; Bishop et al., 1986):

$$\vec{u} = \sum_{r=1}^{m} \vec{u}_r q_r(t) = \sum_{r=1}^{m} (u_r, v_r, w_r) q_r(t) \tag{1a}$$

$$\vec{\theta} = \sum_{r=1}^{m} \vec{\theta}_r q_r(t) = \sum_{r=1}^{m} (\theta_{x,r}, \theta_{y,r}, \theta_{z,r}) q_r(t) \tag{1b}$$

where $\vec{u}_r = (u_r, w_r, v_r)$ and $\vec{\theta}_r = (\theta_{x,r}, \theta_{y,r}, \theta_{z,r})$ denote the translation and rotation, respectively, of each structural node for the rth principal mode and q_r ($r = 1, 2, …, m$) denotes the rth principal coordinate response. Furthermore, the variable r, which ranges in value from 1 to 6, denotes the six rigid motions of the floating structure, namely, surge, sway, heave, roll, pitch and yaw, respectively.

The fluid boundary is made up of a wetted body surface S_b, a free surface S_f, the intersection of a body surface and a free surface Γ, and an infinite boundary surface S_∞. Let $\vec{n}$ denote the normal direction of the body surface towards the inner hull of the ship and let U_0 denote the forward speed of the ship hull.

2.2. Hydrodynamic coefficients and equations of modal response

The radiation potential $\varphi_r(p, t)$ of the rth mode can be decomposed into two transient terms and a memory term. Let

$$\varphi_r(p, t) = \int_0^t \phi_r(p, \tau) \dot{q}_r(t - \tau) d\tau \tag{2a}$$

and

$$\phi_r(p, t) = \psi_{1r}(p)\delta(t) + \psi_{2r}(p)H(t) + \chi_r(p, t) \tag{2b}$$

where $\psi_{1r}(p)$ and $\psi_{2r}(p)$ denote transient terms, $\psi_{2r}(p)$ is relative to forward speed, $\chi_r(p, t)$ is the memory term, $\delta(t)$ and $H(t)$ are the Dirac impulse function and the step function, respectively. Then

$$\varphi_r(p, t) = \psi_{1r}(p)\dot{q}_r(t) + \psi_{2r}(p)q_r(t) + \int_0^t \chi_r(p, t - \tau)\dot{q}_r(\tau)d\tau \tag{2c}$$

The generalized boundary condition of radiation potential on the body's wetted surface may be represented as (Wu, 1984)

$$\frac{\partial \varphi_r(p, t)}{\partial n} = (\vec{u}_r \cdot \vec{n})\dot{q}_r(t) + [\vec{\theta}_r \times \vec{W} \cdot \vec{n} - (\vec{u}_r \cdot \nabla)\vec{W} \cdot \vec{n}]q_r(t) \tag{3a}$$

which can be simplified as follows:

$$\frac{\partial \varphi_r(p, t)}{\partial n} = a_r \dot{q}_r(t) + b_r q_r(t) \tag{3b}$$

In the above expression, $\vec{W} = (W_x, W_y, W_z)$ denotes the velocity of the steady flow relative to the moving equilibrium coordinate system. For a slender, thin, flat, or slowly moving body, it may be simplified as $\vec{W} = (-U_0, 0, 0)$. In this case, the term in Eq. (3b) can be written as

$$b_r = -\frac{U_0}{2}\left[n_2\left(\frac{\partial v_r}{\partial x} - \frac{\partial u_r}{\partial y}\right) - n_3\left(\frac{\partial u_r}{\partial z} - \frac{\partial w_r}{\partial x}\right) \right] = U_0(n_3\theta_{yr} - n_2\theta_{zr}) \tag{3c}$$

or as $b_r = U_0 m_r$, where $m_r = n_3\theta_{yr} - n_2\theta_{zr}$.

The equation of motion in the time domain is derived and expressed in the following form:

$$[a + A]\{\ddot{q}(t)\} + [b + B]\{\dot{q}\} + [c + C + C']\{q\} + \int_0^t [K(t - \tau)]\{\dot{q}(\tau)\}d\tau = \{F\} + \{R'\} \tag{4}$$

where $\{q(t)\}$ denotes the principal coordinate; $[a]$, $[b]$ and $[c]$ are the inertia mass matrix, damping matrix and elastic restoring force matrix, respectively; $[C]$ is the restoring force in still water; $\{F\}$ is the generalized wave exciting force; $\{R'\}$ is the time variant concentrated force, such as a mooring force; $[A]$ and $[K]$ are the added mass and impulse response functions, respectively; and $[B]$ and $[C']$ are the added damping and restoring force, respectively, induced by the forward speed effect, which will vanish for zero speed. The elements of these matrices are as follows:

$$A_{rk} = \rho \iint_{S_b} a_r \psi_{1k} \mathrm{d}S \tag{5a}$$

$$B_{rk} = \rho \iint_{S_b} a_r \psi_{2k} \mathrm{d}S + \rho U_0 \iint_{S_b} \vec{n} \frac{\partial \vec{u}_r}{\partial x} \psi_{1k} \mathrm{d}S \tag{5b}$$

$$C'_{rk} = \rho U_0 \iint_{S_b} \vec{n} \frac{\partial \vec{u}_r}{\partial x} \psi_{2k} \mathrm{d}S \tag{5c}$$

$$K_{rk}(t) = \rho \iint_{S_b} a_r \frac{\partial \chi_k}{\partial t} \mathrm{d}S + \rho U_0 \iint_{S_b} \vec{n} \frac{\partial \vec{u}_r}{\partial x} \chi_k \mathrm{d}S \tag{5d}$$

where ρ denotes fluid density.

3. Radiation potential

The 3D time-domain Green's function in finite water depth is ([Finkelstein, 1957](#))

$$G(p, q, t - \tau) = \overline{G}(p, q)\delta(t - \tau)\tilde{G}(p, q; t - \tau) \tag{6}$$

$$\overline{G}(p, q) = \frac{1}{r} + \frac{1}{r_2} - 2 \int_0^\infty e^{-kh} \frac{\cosh k(z + h)\cosh k(\zeta + h)}{\cosh kh} \mathrm{J}_0(kR)\mathrm{d}k \tag{7a}$$

$$\tilde{G}(p, q; t - \tau) = 2 \int_0^\infty \sqrt{gk \tan h\, kh} \sin\left(\sqrt{gk \tan h\, kh(t - \tau)}\right) \cdot \frac{\cosh k(z + h)\cosh k(\zeta + h)}{\cosh kh \sinh kh} \mathrm{J}_0(kR')\mathrm{d}k \tag{7b}$$

where $R' = \sqrt{[(x - \xi) + U_0(t - \tau)]^2 + (y - \eta)^2}$, $R = \sqrt{(x - \xi)^2 + (y - \eta)^2}$, $r = \sqrt{R^2 + (z - \zeta)^2}$, $r_2 = \sqrt{R^2 + (z + \zeta + 2h)^2}$, h and t denote water depth and time, respectively, $\delta()$, $H()$ and $\mathrm{J}_n()$ are the impulse function, jump function and nth order Bessel function of the first kind, respectively, and $p(x, y, z)$ and $q(\xi, \eta, \zeta)$ denote the field point and the source point, respectively. The two right terms of Eq. [(6)](#) are the transient effect and memory effect, respectively, also called fluctuation effects.

The boundary integral equation of the perturbation velocity potential can be obtained using Stokes' theorem, as follows:

$$2\pi\varphi(p, t) = \iint_{S_b} \left[\overline{G}(p, q) \frac{\partial \varphi(q, t)}{\partial n_q} - \varphi(q, t) \frac{\partial \overline{G}(p, q)}{\partial n_q} \right] \mathrm{d}S_q$$

$$+ \int_{t_0}^t \mathrm{d}\tau \iint_{S_b} \left[\tilde{G}(p, q; t - \tau) \frac{\partial \varphi(q, \tau)}{\partial n_q} - \varphi(q, \tau) \frac{\partial \tilde{G}(p, q; t - \tau)}{\partial n_q} \right] \mathrm{d}S_q$$

$$+ \frac{1}{g} \int_{t_0}^t \mathrm{d}\tau \oint_\Gamma \left\{ U_0^2 \left[\tilde{G}(p, q; t - \tau) \frac{\partial \varphi(q, r)}{\partial \xi} - \varphi(q, \tau) \frac{\partial \tilde{G}(p, q; t - \tau)}{\partial \xi} \right] \right\}$$

$$- U_0 \left\{ \left[\tilde{G}(p, q; t - \tau) \frac{\partial \varphi(q, \tau)}{\partial \tau} - \varphi(q, \tau) \frac{\partial \tilde{G}(p, q; t - \tau)}{\partial \tau} \right] \right\} \mathrm{d}\eta \tag{8}$$

where t_0 is the initial time, which usually equals zero.

3.1. Solution of the Green's function

If the non-dimensional parameters $X = R'/h$, $Y = -z/h$, $Z = -\zeta/h, T = (t - \tau)\sqrt{g/h}$ and $u = kh$ are introduced, the expression of the 3D Green's function for finite water depth becomes

$$G = \frac{1}{h}[F_0(X, Y - Z) + F_0(X, 2 - Y - Z)]$$

$$+ \sqrt{\frac{g}{h^3}}[F(X, Y - Z, T) + F(X, 2 - Y - Z, T)] \tag{9}$$

and

$$F_0(X, V) = \frac{1}{\sqrt{X^2 + V^2}} - \int_0^\infty e^{-u} \mathrm{sech} u \cos(uV)\mathrm{J}_0(uX)\mathrm{d}u \tag{10a}$$

$$F(X, V, T) = \int_0^\infty \sqrt{u \tanh u} \sin\left(T\sqrt{u \tanh u}\right) \frac{\cosh(uV)}{\cosh u \sinh u} \mathrm{J}_0(uX)\mathrm{d}u \tag{10b}$$

where V represents $Y - Z$ or $2 - Y - Z$, and $V \in [-1, 2]$. If both the source point and the field point are on the free surface, V equals 2. When the source point is on the seabed and the field point is on the free surface, V equals -1.

(1) Transient term

Let

$$\overline{G} = \frac{1}{h}[F_0(X, Y - Z) + F_0(X, 2 - Y - Z)] \tag{11a}$$

Then,

$$\frac{\partial \overline{G}}{\partial \xi} = \frac{(\xi - x)}{Rh^2} \left[\frac{\partial F_0(X, Y - Z)}{\partial X} + \frac{\partial F_0(X, 2 - Y - Z)}{\partial X} \right] \tag{11b}$$

$$\frac{\partial \overline{G}}{\partial \eta} = \frac{(\eta - y)}{Rh^2} \left[\frac{\partial F_0(X, Y - Z)}{\partial X} + \frac{\partial F_0(X, 2 - Y - Z)}{\partial X} \right] \tag{11c}$$

$$\frac{\partial \overline{G}}{\partial \zeta} = \frac{1}{h^2} \left[\frac{\partial F_0(X, Y - Z)}{\partial V} + \frac{\partial F_0(X, 2 - Y - Z)}{\partial V} \right] \tag{11d}$$

The approximate solution has been studied in detail using Fourier series ([Newman, 1990](#); [Han et al., 2004](#)). Due to space limitations, it is not listed here.

(2) Memory term

Let

$$\tilde{G} = \sqrt{\frac{g}{h^3}}[F(X, Y - Z, T) + F(X, 2 - Y - Z, T)] \tag{12a}$$

Then,

$$\frac{\partial \tilde{G}}{\partial R'} = \sqrt{\frac{g}{h^5}} \left[\frac{\partial F(X, Y - Z, T)}{\partial X} + \frac{\partial F(X, 2 - Y - Z, T)}{\partial X} \right] \tag{12b}$$

$$\frac{\partial \tilde{G}}{\partial \xi} = -\frac{(x - \xi) + U_0(t - \tau)}{R} \frac{\partial \tilde{G}}{\partial R'} \tag{12c}$$

$$\frac{\partial \tilde{G}}{\partial \eta} = \frac{(\eta - y)}{R} \frac{\partial \tilde{G}}{\partial R'},\tag{12d}$$

$$\frac{\partial \tilde{G}}{\partial \zeta} = \sqrt{\frac{g}{h^5}} \left[\frac{\partial F(X, Y - Z, T)}{\partial V} + \frac{\partial F(X, 2 - Y - Z, T)}{\partial V} \right]\tag{12e}$$

$$\frac{\partial \tilde{G}}{\partial \tau} = -\frac{g}{h^2} \left[\frac{\partial F(X, Y - Z, T)}{\partial T} + \frac{\partial F(X, 2 - Y - Z, T)}{\partial T} \right]$$

$$-U_0 \frac{(x - \xi) + U_0(t - \tau)}{R'} \frac{\partial \tilde{G}}{\partial R'}\tag{12f}$$

$$F = 2 \int_0^\infty \sqrt{u \tanh u} \sin\left(T\sqrt{u \tanh u}\right) \frac{e^{-u(2-V)} + e^{-u(2+V)}}{1 - e^{-4u}} J_0(uX) du\tag{13}$$

The convergence rate of the integral in Eq. (13) can be accelerated by adding and subtracting an appropriate function that is asymptotically equivalent to the integrand for larger u. A judicious choice for this function leads to the following result:

$$F - F_\infty = 2 \int_0^\infty du \left[e^{-2u} \sqrt{u} J_0(uX) \cdot \left[\sqrt{\tanh u} \sin\left(T\sqrt{u \tanh u}\right) \frac{2 \cosh(uV)}{1 - e^{-4u}} \right.\right.$$
$$\left.\left. - \sin\left(T\sqrt{u}\right) e^{u|V|} \right]\right]\tag{14a}$$

As u tends to infinity, the integrand in Eq. (14a) is of order e^{-2u} or smaller. The solution to Eq. (14a) can be obtained by the general integral method. The derivatives of $F - F_\infty$ are

$$\frac{\partial (F - F_\infty)}{\partial X} = -2 \int_0^\infty du \left[e^{-2u} u^{3/2} J_1(uX) \cdot \left[\sqrt{\tanh u} \sin\left(T\sqrt{u \tanh u}\right) \frac{2 \cosh(uV)}{1 - e^{-4u}} \right.\right.$$
$$\left.\left. - \sin\left(T\sqrt{u}\right) e^{u|V|} \right]\right]\tag{14b}$$

$$\frac{\partial (F - F_\infty)}{\partial V} = 2 \int_0^\infty du \left[e^{-2u} u^{3/2} J_0(uX) \right] \cdot \left[\sqrt{\tanh u} \sin\left(T\sqrt{u \tanh u}\right) \frac{2 \sinh(uV)}{1 - e^{-4u}} \right.$$
$$\left. - \sin\left(T\sqrt{u}\right) e^{u|V|} \right]\tag{14c}$$

$$\frac{\partial (F - F_\infty)}{\partial T} = 2 \int_0^\infty du \left[e^{-2u} u J_0(uX) \right] \cdot \left[\tanh u \cos\left(T\sqrt{u \tanh u}\right) \frac{2 \cosh(uV)}{1 - e^{-4u}} \right.$$
$$\left. - \cos\left(T\sqrt{u}\right) e^{u|V|} \right]\tag{14d}$$

When u tends to infinity, the expression of F_∞ is

$$F_\infty = \lim_{u \to +\infty} F = 2 \int_0^\infty \sqrt{u} \sin\left(T\sqrt{u}\right) e^{u(|V|-2)} J_0(uX) du\tag{15a}$$

Its derivatives are

$$\frac{\partial F_\infty}{\partial X} = -2 \int_0^\infty u^{3/2} \sin\left(T\sqrt{u}\right) e^{u(|V|-2)} J_1(uX) du\tag{15b}$$

$$\frac{\partial F_\infty}{\partial V} = 2 \int_0^\infty u^{3/2} \sin\left(T\sqrt{u}\right) e^{u(|V|-2)} J_0(uX) du\tag{15c}$$

$$\frac{\partial F_\infty}{\partial T} = 2 \int_0^\infty u \cos\left(T\sqrt{u}\right) e^{u(|V|-2)} J_0(uX) du\tag{15d}$$

The value F_∞ corresponds to the case of infinite water depth. Yang (2016) gave the solution using a fourth-order ordinary differential equation. If the variables $W = \sqrt{(2 - |V|)^2 + X^2}$, $\mu = \frac{2-|V|}{W}$, $\beta = T/\sqrt{W}$ and $\lambda = uW$ are introduced, the Eq (15a) to (15d) become the following expressions, as in (Yang, 2016, Eq. (3.51) to Eq. (3.53)):
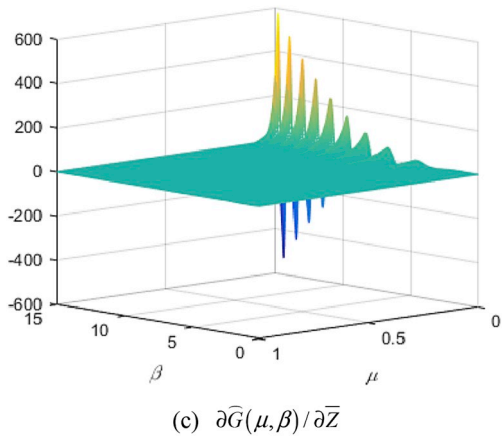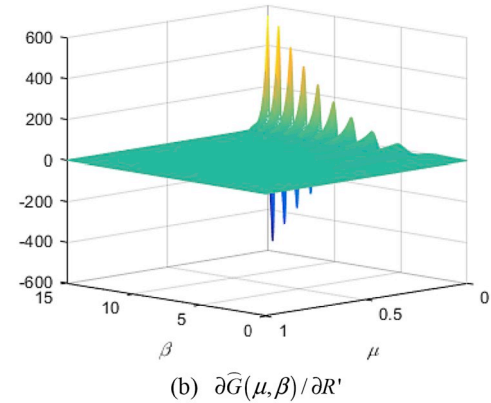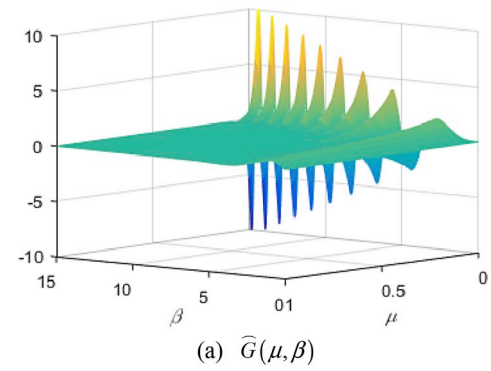

(a) $\widehat{G}(\mu, \beta)$

(b) $\partial \widehat{G}(\mu, \beta) / \partial R'$

(c) $\partial \widehat{G}(\mu, \beta) / \partial \overline{Z}$

Fig. 1. 3D contour of $\partial \widehat{G}(\mu, \beta)$ and its derivatives.

$$F_\infty = \frac{2}{W^{1.5}} \int_0^\infty \sqrt{\lambda} \sin\left(\sqrt{\lambda}\beta\right) e^{-\lambda\mu} J_0\left(\lambda\left(\sqrt{1-\mu^2}\right)\right) d\lambda\tag{16a}$$
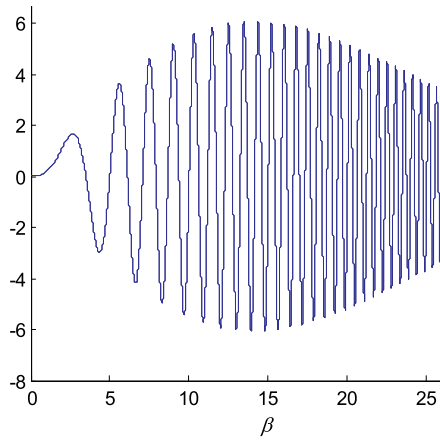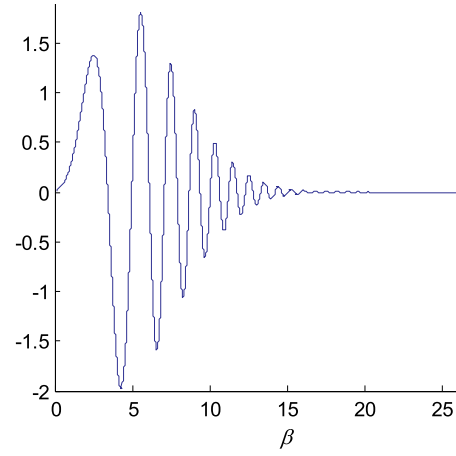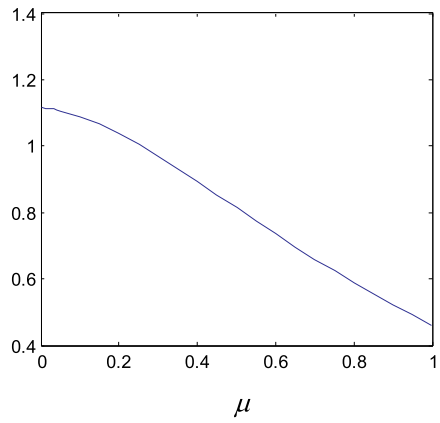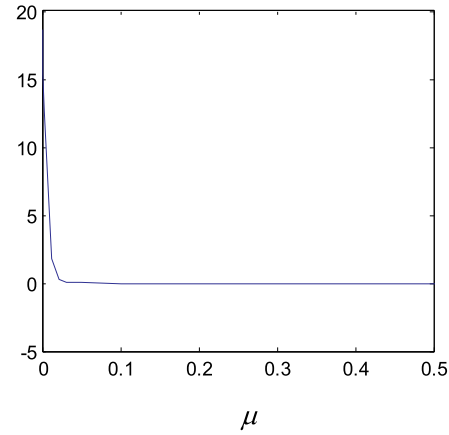
$$\frac{\partial F_\infty}{\partial X} = -\frac{2}{W^{2.5}} \int_0^\infty \sqrt{\lambda^3} \sin\left(\sqrt{\lambda}\beta\right) e^{-\lambda\mu} J_1\left(\lambda\left(\sqrt{1-\mu^2}\right)\right) d\lambda\tag{16b}$$

$$\frac{\partial F_\infty}{\partial V} = \frac{2}{W^{2.5}} \int_0^\infty \sqrt{\lambda^3} \sin\left(\sqrt{\lambda}\beta\right) e^{-\lambda\mu} J_0\left(\lambda\left(\sqrt{1-\mu^2}\right)\right) d\lambda\tag{16c}$$

$$\frac{\partial F_\infty}{\partial T} = \frac{2}{W^2} \int_0^\infty \lambda \cos\left(\sqrt{\lambda}\beta\right) e^{-\lambda\mu} J_0\left(\lambda\left(\sqrt{1-\mu^2}\right)\right) d\lambda\tag{16d}$$

The following new variables are introduced for determining the values in Eq. (16a) to Eq. (16d):

$$\widehat{G}(\mu, \beta) = \int_0^\infty \sqrt{\lambda} \sin\left(\sqrt{\lambda}\beta\right) e^{-\lambda\mu} J_0\left[\lambda\left(\sqrt{1-\mu^2}\right)\right] d\lambda\tag{17a}$$

(a) $G(\mu, \beta)$ ($\mu = 0.01$)

(b) $G(\mu, \beta)$ ($\mu = 0.1$)

(c) $G(\mu, \beta)$ ($\beta = 2$)

(d) $G(\mu, \beta)$ ($\beta = 28$)

Fig. 2. The values of $\widehat{G}(\mu, \beta)$

$$\widehat{G}_{R'}(\mu, \beta) = \int_0^\infty \sqrt{\lambda^3} \sin\left(\sqrt{\lambda}\,\beta\right) e^{-\lambda\mu} J_1\left[\lambda\left(\sqrt{1-\mu^2}\,\right)\right] d\lambda \tag{17b}$$

$$\widehat{G}_{\overline{Z}}(\mu, \beta) = \int_0^\infty \sqrt{\lambda^3} \sin\left(\sqrt{\lambda}\,\beta\right) e^{-\lambda\mu} J_0\left[\lambda\left(\sqrt{1-\mu^2}\,\right)\right] d\lambda \tag{17c}$$

$$\widehat{G}_\beta(\mu, \beta) = \int_0^\infty \lambda \cos\left(\sqrt{\lambda}\,\beta\right) e^{-\lambda\mu} J_0\left(\lambda\left(\sqrt{1-\mu^2}\,\right)\right) d\lambda \tag{17d}$$

where $\overline{Z} = z + \zeta$, and $\widehat{G}_{R'}(\mu, \beta)$, $\widehat{G}_{\overline{Z}}(\mu, \beta)$ and $\widehat{G}_\beta(\mu, \beta)$ are the first order partial derivatives of R', $\overline{Z}$ and β, respectively.
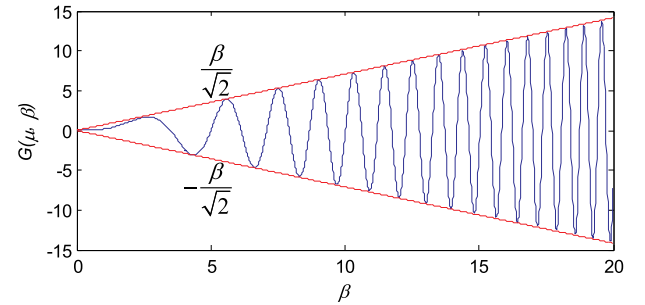
The new notation $\partial^{(n)} F / \partial\beta^{(n)} = F^{(n)}$ is introduced. The term $\widehat{G}(\mu, \beta)$ satisfies a fourth-order ordinary differential equation in the independent variable β (Clement, 1998), which can be solved by the fourth-order Runge-Kutta method:

$$\widehat{G}^{(4)} + \mu\beta\widehat{G}^{(3)} + \left(\frac{\beta^2}{4} + 4\mu\right)\widehat{G}^{(2)} + \frac{7}{4}\beta\widehat{G}^{(1)} + \frac{9}{4}\widehat{G} = 0 \tag{18}$$

Then, the values of the terms in Eq. (17a) to Eq. (17d) can be obtained by

$$\widehat{G}_{R'}(\mu, \beta) = \frac{1}{\sqrt{1-\mu^2}} \left[\frac{3}{2}\widehat{G}(\mu, \beta) + \frac{\beta}{2}\widehat{G}^{(1)}(\mu, \beta) + \mu\widehat{G}^{(2)}(\mu, \beta)\right] \tag{19a}$$

$$\widehat{G}_{\overline{Z}}(\mu, \beta) = -\widehat{G}^{(2)}(\mu, \beta) \tag{19b}$$
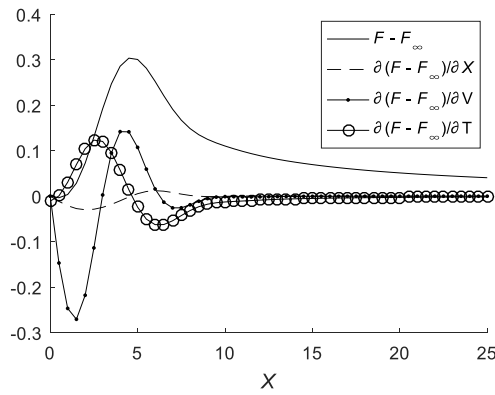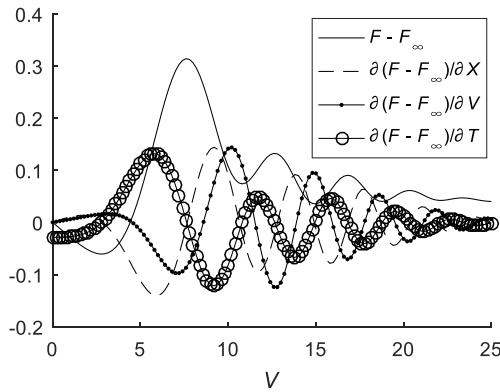

Fig. 3. The values of $\widehat{G}(0, \beta)$

$$\widehat{G}_\beta(\mu, \beta) = \widehat{G}^{(1)}(\mu, \beta) \tag{19c}$$

Finally, the values of F and its derivatives can be determined by Eq (14a) to (15d).

3.2. Numerical results of the Green's function

The computations in this paper show that when the fourth-order Runge-Kutta method is applied, a stable value can be obtained with a time step of 0.001. The non-dimensional Green's function $\widehat{G}(\mu, \beta)$ and its

5

(a) $V = 0.5$

(b) $X = 5$

Fig. 4. The value of $F - F_\infty$ and its derivatives ($T = 1.0$).

derivatives are shown in Fig. 1 and Fig. 2. It is shown that at time $\mu = 0$ (when the source point and the field point are both on the free surface), the Green's function and its derivatives oscillate sharply with increasing values of the non-dimensional time variable β. When μ becomes larger, the Green's function and its derivatives decrease with increasing values of β. Finally, these values tend toward zero, and the larger μ is, the faster these values tend toward zero.

When $\mu = 0$, the oscillation of the Green's function and its derivatives increases with an increasing non-dimensional time, and the stability of the calculation results become very important. The analytical expression of $\widehat{G}(0, \beta)$ is as follows (Clement, 1998):

$$\widehat{G}(0, \beta) = \frac{\pi\beta}{2\sqrt{2}} \left[J_{1/4}\left(\frac{\beta^2}{8}\right) J_{-1/4}\left(\frac{\beta^2}{8}\right) + J_{3/4}\left(\frac{\beta^2}{8}\right) J_{-3/4}\left(\frac{\beta^2}{8}\right) \right] \frac{\beta^2}{8} \tag{20}$$

It can be concluded that when $\beta \to +\infty$, $\widehat{G}(0, \beta)$ is always between the asymptotes of $\pm\beta/\sqrt{2}$. The numerical results for $\beta = [0, 20]$ are given in Fig. 3. The calculation results in this paper are in good agreement with the analytical solution, which shows that the numerical results are stable.

The variation in non-dimensional time and its derivatives with respect to X and V when T equals 1.0 is shown in Fig. 4 and Fig. 5, respectively. The results show that the contours of $F - F_\infty$ and its derivative with respect to X are more intense and have greater oscillatory attenuation, while the contours of $F - F_\infty$ and its derivatives with respect to V are gentler.

The results in Fig. 6 show that when V remains unchanged, $F - F_\infty$

and its derivative vary dramatically with T and take many oscillations to attenuate. The X is larger; the more time is needed for attenuation. In addition, the larger the horizontal scale of the floating body is, the longer it takes for the time axis of the Green's function to be calculated, and the more time elapses.

The results in Fig. 7 show that when X remains unchanged, $F - F_\infty$ and its derivative vary dramatically with T and take many oscillations to attenuate. However, for different values of V, the oscillation attenuation times are almost the same. It can be concluded that the amount of time needed to calculate the time axis of the Green's function does not change much when the vertical scale of the floating body increases.

4. Incident force and diffraction force

4.1. Incident velocity potential

The incident wave direction β is defined in Fig. 8. The 0° and 180° denote the following sea and heading sea, respectively. The first-order formula of the instantaneous height of the incident wave is

$$\zeta = Ae^{ik(x \cos \beta + y \sin \beta) - i\omega t} \tag{21a}$$

where the variables A, k and ω denote the wave amplitude, wave number and natural wave frequency, respectively. In addition, $\nu = \omega^2/g$ and $k \tanh kh = \nu$.

The first order formula of incident velocity potential Φ_I in the equilibrium coordinate system is

$$\Phi_I = \text{Re}\left[\varphi_I e^{-i\omega t}\right] = \text{Re}\left[\frac{Ag}{i\omega} \frac{\cosh k(z + h)}{\cosh kh} e^{ik(x \cos \beta + y \sin \beta) - i\omega t}\right] \tag{21b}$$

where φ_I, h and g denote the amplitude of the incoming potential of fluid, the water depth and the gravitational acceleration constant, respectively.

4.2. Diffraction velocity potential

The boundary condition of the diffraction potential of the body surface is.

$$\frac{\partial \varphi_D(p, t)}{\partial n} = \frac{-1}{\pi} \text{Re}\left\{ \int_0^\infty \left[(n_1 \cos \beta + n_2 \sin \beta)\cosh k(z + h)\right.\right.$$
$$\left. -n_3 i \cdot \sinh k(z + h)\right] \left[\omega - \omega^2 \frac{2U_0 \cos \beta}{g\left(\tanh kh + kh \text{sech}^2 kh\right)}\right]$$
$$\left. \cdot \frac{e^{ik\alpha}}{\sinh kh} e^{-i(\omega - kU_0 \cos \beta)t} d\omega \right\} \tag{22a}$$

The convergence rate of the integral in Eq. (22a) can be accelerated by adding and subtracting an appropriate function that is asymptotically equivalent to the integrand for larger ω. A judicious choice of this function leads to the following results:

$$\frac{\partial \varphi_D(p, t)}{\partial n} - \lim_{\omega \to +\infty} \frac{\partial \varphi_D(p, t)}{\partial n} = \frac{-1}{\pi} \text{Re}\left\{ \int_0^\infty \{[(n_1 \cos \beta + n_2 \sin \beta)\right.$$
$$\cdot \frac{\cosh k(z + h)}{\sinh kh} - n_3 i \cdot \frac{\sinh k(z + h)}{\sinh kh}\right] \left[\omega - \omega^2 \frac{2U_0 \cos \beta}{g\left(\tanh kh + kh \text{sech}^2 kh\right)}\right]$$
$$\left. -(n_1 \cos \beta + n_2 \sin \beta - n_3 i)\left(\omega - \omega^2 \frac{2U_0 \cos \beta}{g}\right) e^{kz}\right\}$$
$$\left. \cdot e^{ik\alpha} e^{-i(\omega - kU_0 \cos \beta)t} d\omega \right\} \tag{22b}$$

When ω tends to infinity, the expression of $\lim_{\omega \to +\infty} \frac{\partial \varphi_D(p, t)}{\partial n}$ is

$$\lim_{\omega \to +\infty} \frac{\partial \varphi_D(p,t)}{\partial n} = \frac{-1}{\pi} \text{Re} \left[(n_1 \cos \beta + n_2 \sin \beta - n_3 i) \cdot \int_0^{\infty} \left(\omega - \omega^2 \frac{2U_0 \cos \beta}{g} \right) e^{k(z+i\alpha)} e^{-i(\omega - kU_0 \cos \beta)t} d\omega \right] \tag{22c}$$

The above formula is the value of infinite water depth, and the solving method was derived in the literature (Wang, 1996; Yang, 2016).

Finally, the equation of diffraction potential $\varphi_D(p,t)$ is solved:

$$2\pi\varphi_D(p,t) + \iint_{S_b} \varphi_D(q,t) \frac{\partial}{\partial n_q} \left(\frac{1}{r} - \frac{1}{r_1} \right) dS_q = \iint_{S_b} \left(\frac{1}{r} - \frac{1}{r_1} \right) \frac{\partial \varphi_D(q,t)}{\partial n_q} dS_q$$

$$+ \int_{-\infty}^{t} d\tau \iint_{S_b} \left[\tilde{G}(p,q;t-\tau) \frac{\partial \varphi_D(q,\tau)}{\partial n_q} - \varphi_D(q,\tau) \frac{\partial}{\partial n_q} \tilde{G}(p,q;t-\tau) \right] dS_q$$

$$- \frac{1}{g} \int_{-\infty}^{t} d\tau \oint_{\Gamma} \left\{ U_0^2 \left[\tilde{G}(p,q;t-\tau) \frac{\partial \varphi_D(q,\tau)}{\partial \xi} - \varphi_D(q,\tau) \frac{\partial}{\partial \xi} \tilde{G}(p,q;t-\tau) \right] \right.$$

$$\left. - U_0 \left[\tilde{G}(p,q;t-\tau) \frac{\partial \varphi_D(q,\tau)}{\partial \tau} - \varphi_D(q,\tau) \frac{\partial}{\partial \tau} \tilde{G}(p,q;t-\tau) \right] \right\} d\eta \tag{23}$$

Since the diffraction potential and its derivative have gone to zero before a certain negative time, the actual calculation does not need to start from negative infinity; selecting an appropriate negative time is sufficient.

### 4.3. Wave exciting force and impulse response function

According to the linear system and impulse response theory, the wave exciting force of the rth mode generated by any incident wave is defined as

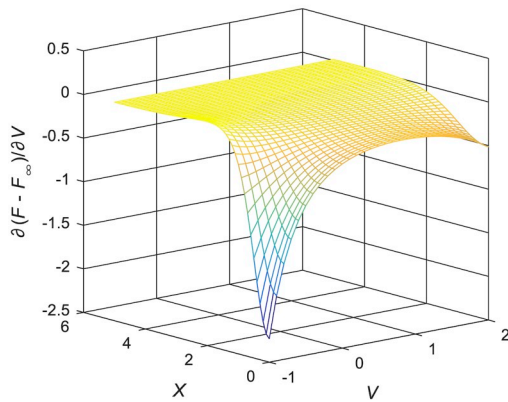$$F_r(t) = \int_{-\infty}^{\infty} [K_{ro}(t-\tau) + K_{rD}(t-\tau)]\zeta_0(\tau) d\tau \tag{24}$$

where $K_{ro}(t)$ and $K_{rD}(t)$ denote the impulse response function of the incident wave and the diffraction wave, respectively, induced by the instantaneous impulse wave $\delta(t)$ at $t = 0$. Let
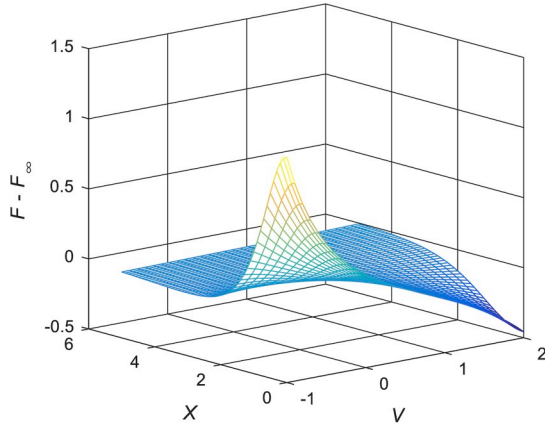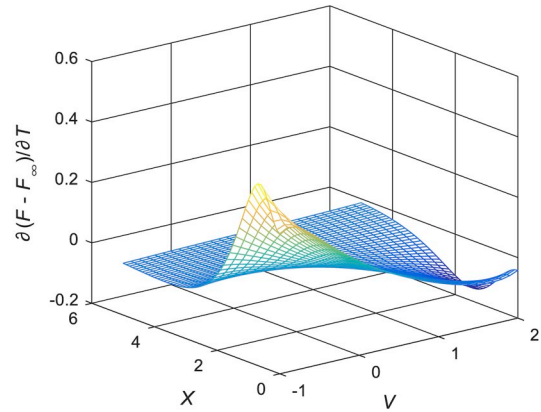

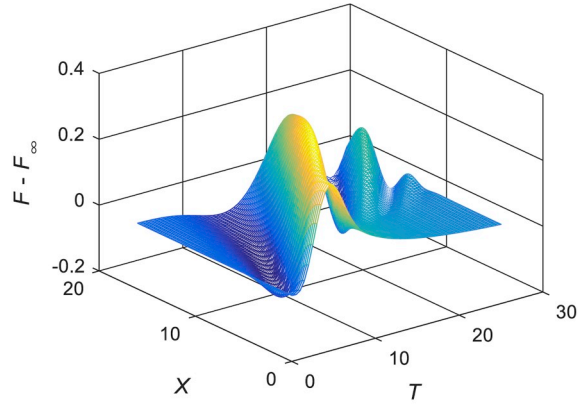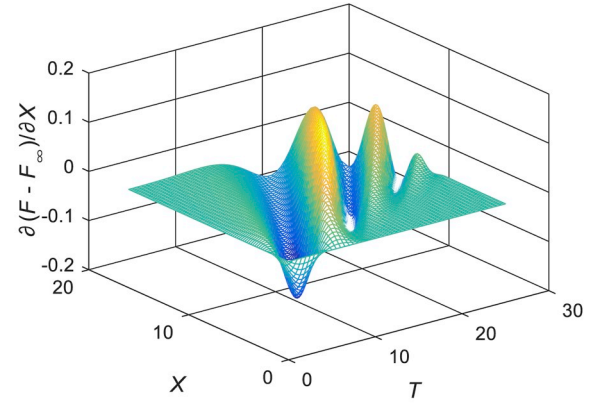(a) The value of $F - F_\infty$
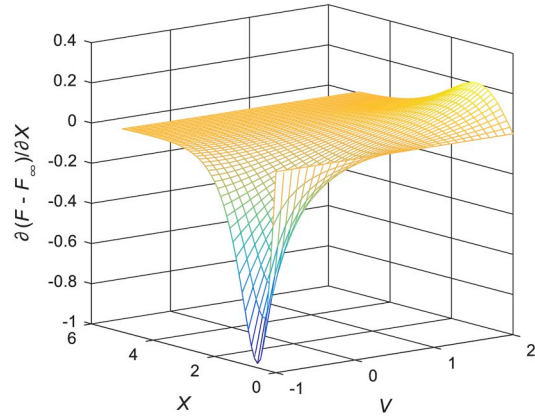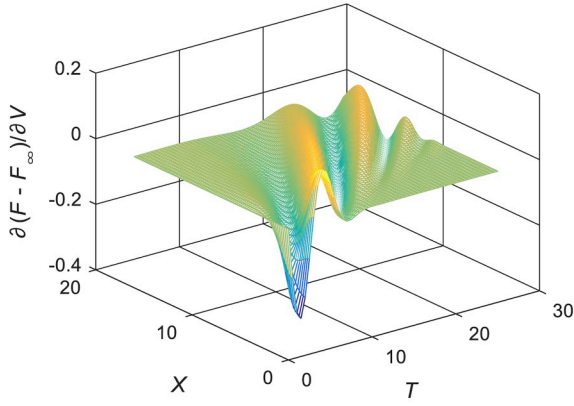

(b) The partial derivative to X

(c) The partial derivative to V

(d) The partial derivative to T

Fig. 5. 3D contour of $F - F_\infty$ and its derivatives ($T = 1.0$).
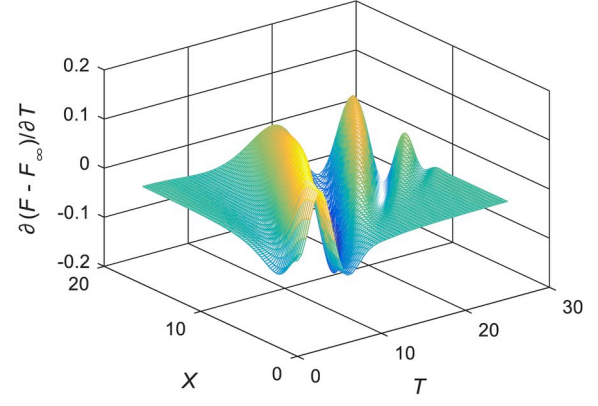
(a) The value of $F - F_\infty$

(b) The partial derivative to X

(c) The partial derivative to V

(d) The partial derivative to T

Fig. 6. 3D contour of $F - F_\infty$ and its derivatives ($V = 0.5$).

$$K_r(t) = \iint_{S_b} \vec{n} \cdot \vec{u}_r \widehat{p}(P, t) dS = \iint_{S_b} a_r \widehat{p}(P, t) dS \tag{25}$$

where $\widehat{p}(P, t)$ denotes the pulsating pressure on the wetted body induced by the incident wave or the diffraction wave.

(1) Incident wave exciting force

Let

$$\widehat{p}(P, t) - \lim_{\omega \to +\infty} \widehat{p}_0(P, t) = \frac{\rho g}{\pi} \mathrm{Re} \left\{ \int_0^\infty \left\{ \frac{\cosh k(z + h)}{\cosh kh} \right. \right.$$
$$\left. \cdot \left[\omega - \omega^2 \frac{2 U_0 \cos \beta}{g (\tanh kh + kh \mathrm{sech}^2 kh)} \right] - e^{kz} \left(\omega - \omega^2 \frac{2 U_0 \cos \beta}{g} \right) \right\}$$
$$\left. \cdot e^{\mathrm{i} k\alpha} e^{-\mathrm{i}(\omega - kU_0 \cos \beta)t} d\omega \right\} \tag{26b}$$

When ω tends to infinity, the expression of $\lim_{\omega \to +\infty} \widehat{p}(P, t)$ is

$$\widehat{p}(P, t) = \frac{\rho g}{\pi} \mathrm{Re} \left[\int_0^\infty \frac{\cosh k(z + h)}{\cosh kh} e^{\mathrm{i} k\alpha} \cdot \left(1 - \omega \cdot \frac{2 U_0 \cos \beta}{g (\tanh kh + kh \mathrm{sech}^2 kh)} \right) e^{-\mathrm{i}(\omega - kU_0 \cos \beta)t} d\omega \right] \tag{26a}$$

The convergence rate of the integral in Eq. (26a) can be accelerated by adding and subtracting an appropriate function that is asymptotically equivalent to the integrand for larger ω. A judicious choice of this function leads to the following results:

$$\lim_{\omega \to +\infty} \widehat{p}(P, t) = \frac{\rho g}{\pi} \mathrm{Re} \left[\int_0^\infty \left(\omega - \omega^2 \frac{2 U_0 \cos \beta}{g} \right) \cdot e^{k(z + \mathrm{i}\alpha)} e^{-\mathrm{i}(\omega - kU_0 \cos \beta)t} d\omega \right] \tag{26c}$$

The above formula is simply the value of infinite water depth, and the solving method was derived in the literature (Wang, 1996; Yang,
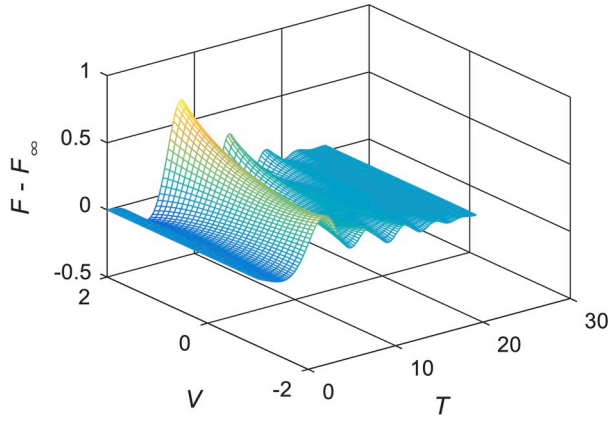
(a) The value of $F - F_\infty$
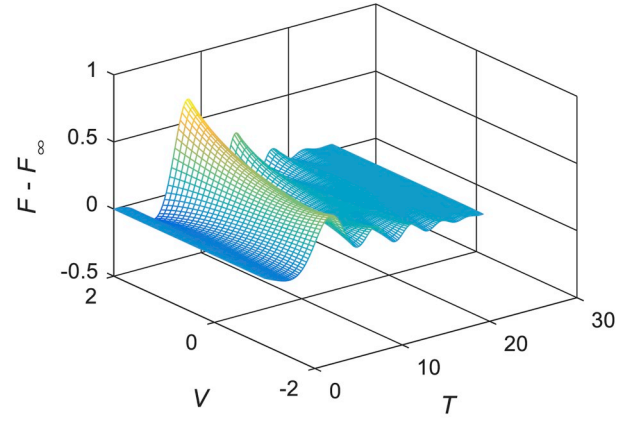
(b) The partial derivative to X
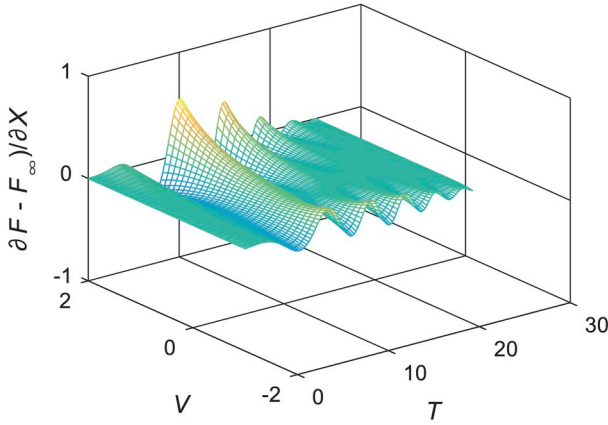
(c) The partial derivative to V
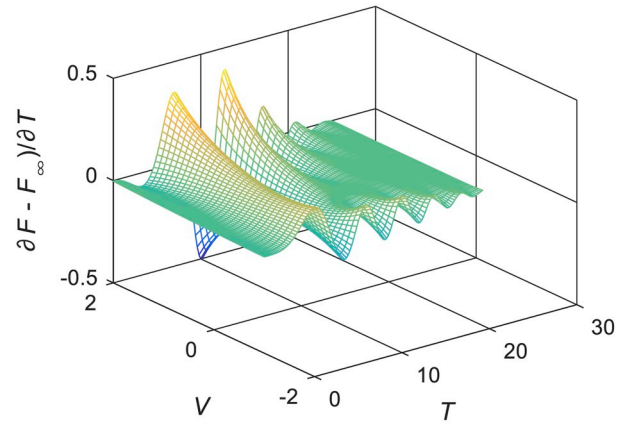
(d) The partial derivative to T

Fig. 7. 3D contour of $F - F_\infty$ and its derivatives ($X = 5$).

2016).

The impulse response function of the incident wave can be obtained by substituting Eq. (26a) into Eq. (25).

(2) Diffraction wave exciting force

If the assumption is made that the body surface at the waterline is a straight wall or an approximately straight wall, then $\overrightarrow{l} \times \overrightarrow{n}$ is perpendicular to $\overrightarrow{W}$. When $\overrightarrow{W} = (-U_0, 0, 0)$, the formula of $K_{rD}(t)$ is simplified as follows:

$$K_{rD}(t) = -\rho \iint\limits_{S_b} a_r \frac{\partial \varphi_{D\delta}}{\partial t} dS - \rho U_0 \iint\limits_{S_b} \varphi_{D\delta} \left(\overrightarrow{n} \cdot \frac{\partial \overrightarrow{u}_r}{\partial x} \right) dS \quad (27)$$

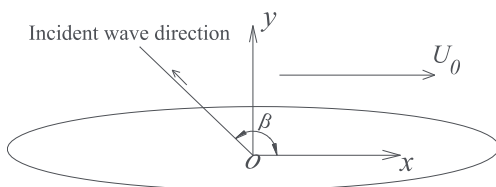Finally, all of the terms of the wave exciting force $F_r(t)$ in Eq. (24) have been established.

Fig. 8. Sketch of the wave direction.

5. Verification and analysis of the results

5.1. Basic information

A bulk carrier is taken as an example in this paper for time domain analysis of wave and structural responses. The dead weight of the ship is 205,000 tons. The model test of the ship under full loading conditions was carried out at the wave basin of the China Ship Scientific Research Center (CSSRC). The scale of the segmented model was 1:50, and the model was made of FRP (fibre reinforced plastic) with ten segments and elastic backbone, as shown in Fig. 9. The 10 segments were cut at stations No. 2, 4, 6, 8, 10 (−50 mm), 12, 14, 16 and 18. In the model test, the wave height was 0.04 m for all regular wave cases.

To examine the loads and the structural responses of the ship in waves, the geometric similarity of the wetted surface, the hydrodynamic similarity of global motions, and the similarities of the mass and stiffness distributions of the hull girder along the length were analysed, together with the radius of longitudinal gyration. The principal details of the ship and the model are listed in Table 1. The resonant frequency of the two-node bending mode in calm water was calculated by employing the software THAFTS for frequency domain three-dimensional hydroelastic analysis; this software was developed by CSSRC based on the 3D theory of the frequency domain (Wu, 1984).

The resonant frequency and damping ratio of the two-node bending mode of the model in calm water without speed were measured in the hammering test. The numerical predictions and the results of the model test are compared in Table 2. The relative error between the two results
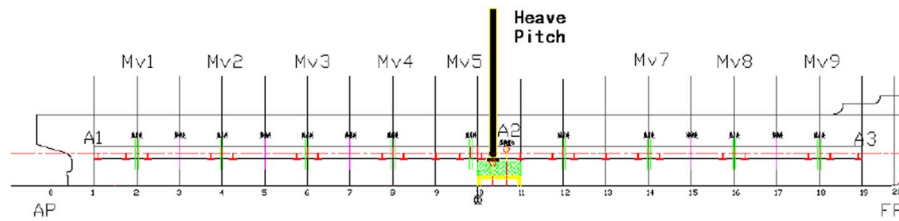
Fig. 9. Measured points of motion and bending moment.

Table 1
The principal details of the bulk carrier.

Parameters	Prototype	Model
L_{BP} (m)	295.0	5.9
Broad (m)	50.0	1.0
Depth (m)	24.7	0.494
Forward draft T_f (m)	17.71	0.354
After draft T_a (m)	18.73	0.375
Displacement (t)	235610.1	1.839
Design speed	14.8 (Kn)	1.077 (m/s)
Water depth (m)	200.0	4.0

Table 2
Predicted and measured two-node frequencies of the model (full scale).

Item	Value
Prediction (rad/s) (a)	2.80
Measured data (rad/s) (b)	2.68
Relative error (%) ((a-b)/b)	4.48

of the two-node frequency is approximately 4.48%. The damping ratio of the two-node elastic mode is 4.55% in the model test, which includes the added damping effect, the hydrodynamic viscous effect and the structural damping effect. The hydrodynamic viscous effect and structural damping ratio are taken to be 1% in the following numerical simulation.

5.2. Numerical calculation and results

The 3D FEM model of the ship hull has 178157 shell elements, 124032 beam elements and 302189 elements in total. The symmetry property of the ship allows the hydroelastic responses to be numerically calculated using half of the wetted surface constituted with a mesh of 794 panels, as shown in Fig. 10 (a). This model is used in the predictions made by the TDGF (Time Domain Green's Function) method.

In the predictions made by the IORM (Inner and Outer Region Matching) method in the time domain (Yang, 2016), a control surface combining a circular cylinder of radius 450 m and a flat bottom is introduced. Similarly, the mesh of the half boundary of the inner fluid region Ω_I consists of 1200 panels on the semi-circle free surface and 672 panels on the half control surface, as shown in Fig. 10 (b).

The 3D FEM model of the bulk carrier in a vacuum is used to calculate the dry global modes and corresponding natural frequencies. Fig. 11 shows the models of two-node vertical bending, one-node torsion, two-node horizontal bending, and three-node vertical bending with full scale natural frequencies from 3.768 rad/s to 7.632 rad/s.

When the ship floats on the water surface and encounters sinusoidal excitations, its structural dynamic responses may contain contributions from different modes. At special exciting frequencies, there are structural resonances. Due to fluid-structure interactions, the hydrodynamic effect appears as the added mass, causing each of the resonant frequencies to be lower than the natural frequencies of the ship, as shown in Table 3. Clearly, it is important to avoid the resonant frequencies lying in the major frequency regions of the engine and the machinery excitations when designing the ship structure. The smallest resonant frequency of the bulk carrier among all structural distortion modes corresponds to the two-node vertical bending mode, which is 2.8 rad/s. Although the frequency region of major wave energy in the sea is usually lower than 1.5 rad/s, the high forward speed of the ship may increase the encounter wave frequency and reach as high as the resonant frequency of the two-node vertical bending mode, resulting in springing responses.

In this section, the motions and wave loading of the bulk carrier are predicted by the TDGF and IORM methods. The predicted impulse response function, the transfer functions of motions and the wave load of the ship advancing in waves at 14.8 kn are compared under the three methods in Fig. 12, along with the model test results. The two time-domain methods provide the results of the impulse response function of heave with good agreement, as shown in Fig. 12 (a). The impulse response function approaches zero when the non-dimensional time is larger than 3.0. The impulse response function of heave predicted by the TDGF method fluctuates slightly when the non-dimensional time is

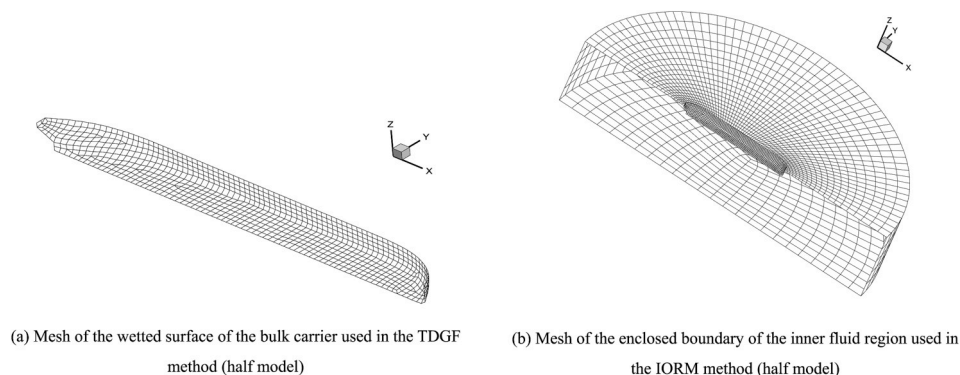(a) Mesh of the wetted surface of the bulk carrier used in the TDGF method (half model)

(b) Mesh of the enclosed boundary of the inner fluid region used in the IORM method (half model)

Fig. 10. Mesh used in the hydroelastic analysis of the bulk carrier.

(a) Two-node vertical bending
(3.768 rad/s)

(b) One-node torsion (4.354 rad/s)

(c) Two-node horizontal bending
(5.253 rad/s)

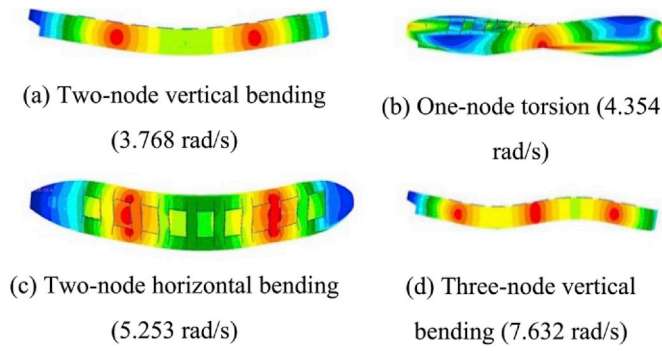(d) Three-node vertical bending (7.632 rad/s)

Fig. 11. Dry modal shapes of the bulk carrier.

Table 3
Natural frequencies and resonant frequencies.

Type	Natural frequency (rad/s)	Resonant frequency (rad/s)
Heave	–	0.547
Roll	–	0.512
Pitch	–	0.600
Two-node vertical bending	3.768	2.800
One-node torsion	4.354	4.032
Two-node horizontal bending	5.253	4.570
Three-node vertical bending	7.632	5.533

greater than 1.0. The reason for this finding requires further investigation. As shown in Fig. 12 (b) and 12 (c), the numerical and experimental results of heave and pitch at 14.8 kn show similar tendencies, except in the encounter frequency region from 0.5 rad/s to 0.6 rad/s. This is the

frequency region of heave and pitch resonances. The numerical predictions by any approaches around this region are usually influenced by the damping effect, including viscous damping; in the model test, the wave height is 0.04 m for all of the regular wave cases. In addition, there is a small amount of spraying in the range of 0.5–0.6 rad/s, which may influence the experimental results. It seems that the numerical results agree well with the model test results in Fig. 12 (b) ~ Fig. 12 (d). In the area labelled S1, where the ratio of wave length to ship length is approximately 1.0, the predictions of TDGF and IORM and the experimental results for the vertical bending moment all decrease, while the prediction of the frequency domain method does not.

For the two time-domain methods, the hydrodynamic panel models of the wetted surface are the same. However, one is a Rankine source on the wetted body, and the other is the Green's function. Therefore, the impulse response functions of the hydrodynamic coefficients and the diffraction force differ somewhat. Thus, the heave and pitch responses are slightly different in some cases.

In the VBM plots, the peak at 2.8 rad/s is due to the linear springing response. The present method predicts lower springing responses compared to THAFTS and IORM. There are two reasons for this result: (1) the peak at 2.8 rad/s is the resonant point, which is more sensitive to damping and exciting forces; and (2) the three methods are based on the difference principle. The hydrodynamic coefficients and diffraction force have a certain level of difference, meaning that their linear springing responses are different.

6. Conclusions

Based on the boundary element method and the superposition principle of structural elastic modes, the three-dimensional time-domain Green's function in finite water depth is applied to hydroelasticity to address more complex problems. Focusing on the difficulties and
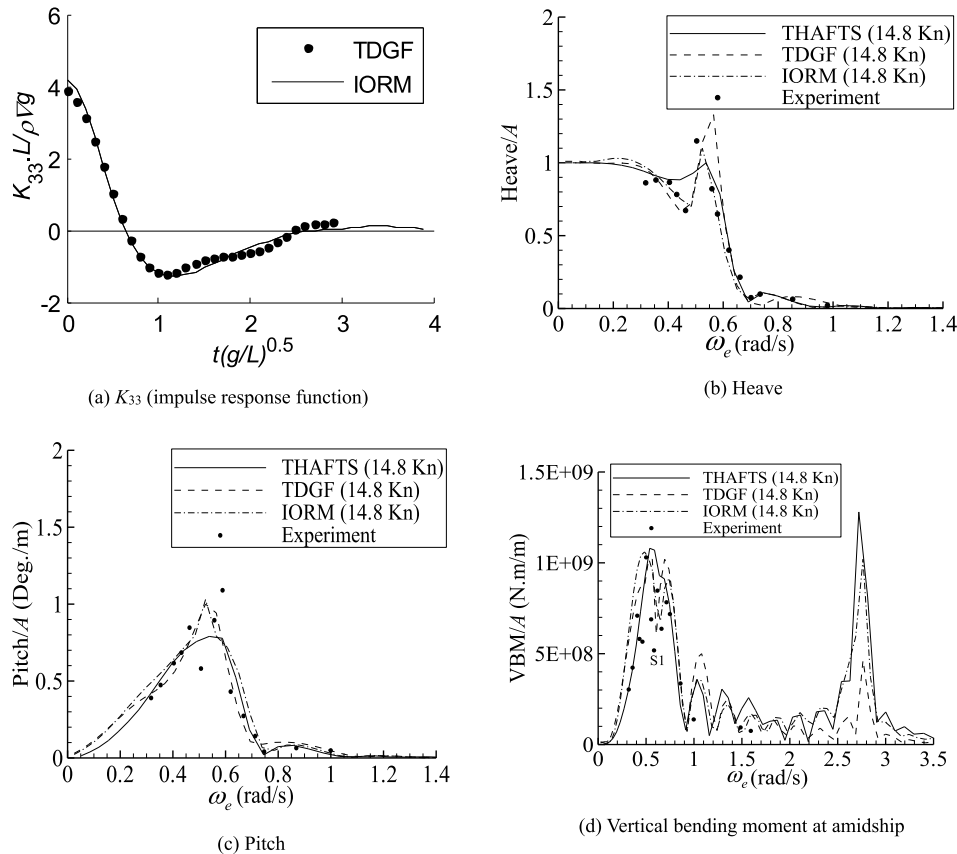

(a) K_{33} (impulse response function)

(b) Heave

(c) Pitch

(d) Vertical bending moment at amidship

Fig. 12. Transfer functions of rigid motions and the vertical bending moment of the bulk carrier (head sea, 14.8 kn).

divergence of the three-dimensional time-domain Green's function in finite water depth, a numerical solution method that has high accuracy and good stability is developed using series expansion, asymptotic methods and fourth-order differential equations. The numerical results obtained by the present method for a large bulk carrier are compared with the results of other numerical methods and verified by the towing model test. Some important conclusions are as follows:

(1) The numerical analysis shows that the time interval of the fourth-order differential equation is 0.001, and the fourth-order Runge-Kutta method can obtain stable and high-precision numerical results.

(2) $F - F_\infty$ and its derivatives with respect to X are more intense and have greater oscillatory attenuation, while $F - F_\infty$ and its derivatives with respect to V are gentler. The larger the horizontal scale of the floating body, the longer it takes for the time axis of the Green's function to be calculated, and the more time elapses. However, the amount of time needed to calculate the time axis of the Green's function does not change much when the vertical scale of the floating body increases.

(3) The convergence rate of the integral of the Green's function, the incident potential and the diffraction boundary condition in finite water depth can be accelerated by adding and subtracting an appropriate asymptotically equivalent function.

(4) The impulse response function approaches zero when the non-dimensional time is larger than 3.0 for the bulk carrier with a forward speed of 14.8 kn. The time-domain method provides results that are in good agreement with the experimental data. When the ratio of wave length to ship length is approximately 1.0, the predictions of TDGF and IORM and the experimental results for the vertical bending moment all decrease, while the prediction of the frequency domain method does not.

Acknowledgment

References

Bishop, R.E.D., et al., 1986. A general linear hydroelasticity theory of floating structures moving in a seaway. Phil. Trans. R. Soc. Lond. A 316, 375–426.

Chen, X.,J., 2001. Second Order Nonlinear Hydroelastic Analysis of Floating Systems (Doctoral thesis,). China Ship Scientific Research Center, Wuxi, China (In Chinese).

Clement, A.H., 1998. An ordinary differential equation for green function of time-domain free-surface hydrodynamics. J. Eng. Math. 33 (2), 201–217.

Ding, J., et al., 2017. Hydroelastic analysis and model tests of a single module VLFS deployed near islands and reefs. Ocean. Eng. 144, 224–234.

Ding, J., et al., 2019. A simplified method to estimate the hydroelastic responses of VLFS in the inhomogeneous waves. Ocean. Eng. 172, 434–445.

Du, S.,X., 1996. A Complete Frequency Domain Analysis Method of Linear Three-Dimensional Responses of Floating Structures in Waves (Doctoral thesis,). China Ship Scientific Research Center, Wuxi, China (In Chinese).

Finkelstein, A.B., 1957. The initial value problem for transient water waves. Commun. Pure Appl. Math. 10, 511–522.

Fu, S.X., Moan, T., 2012. Dynamic analyses of floating fish cage collars in waves. Aquacult. Eng. 47, 7–15.

Han, L., Teng, B., Gou, Y., 2004. Approximation of time-domain Green's function in finite water depth. J. Hydrodyn. Ser. A. 19 (5), 629–636.

Hu, J.J., et al., 2012. Hydroelastic analysis and model tests on the structural response and fatigue behaviours of an ultra-large ore carrier in waves. J. Eng. Marit. Environ. 226 (2), 135–155.

Ikoma, T., Maeda, H., Masuda, K., 1998. Effects of second-order hydroelastic responses on Pontoon type Mega-Float. Proc. OMAE98 43–46.

Li, L., et al., 2013. Dynamic responses of floating fish cage in waves and current. Ocean. Eng. 72 (7), 297–303.

Liu, S.,K., Papanikolaou, A.,D., 2011. Time-domain hybrid method for simulating large amplitude motions of ships advancing in waves. Int. J. Nav. Archit. Ocean. Eng. 3, 72–79.

Liu K., S., Papanikolaou D., A., Duan Y., W., 2006. A time domain numerical simulation method for nonlinear ship motions. J. Harbin Inst. Technol. 27, 177–185.

Maeda, H., Masuda, K., Ikoma, T., 1997. Hydroelastic responses of Pontoon type very large floating offshore structure (The 3rd report), the effects of 2nd–order Wave loads. J. Soc. Nav. Archit. Jpn. 182, 319–328.

Newman, J.N., 1990. The approximation of free-surface Green functions. In: Wave Asymptotic: Proceeding of the Fritz Ursell Retirement Meeting. Cambridge University Press, pp. 107–135.

Nguyen, H.P., et al., 2019. Extracting energy while reducing hydroelastic responses of VLFS using a modular raft wec-type attachment. Appl. Ocean Res. 84, 302–316.

Price, W.G., Wu, Y.S., 1984. Hydroelasticity of marine structure. In: The 16th in. Congress of Theoretical and Applied Mechanics (IUTAM). Lyngby, Denmark.

Tian, C., Wu, Y.S., 2006. The second-order hydroelastic analysis of a SWATH ship moving in large-amplitude waves. J. Hydrodyn. Ser. B. 18 (6), 631–639.

Wang, D.Y., 1996. Three-dimensional Hydro-Elastic Analysis of Ships in Time Domain (Doctoral thesis). China Ship Scientific Research Center, Wuxi, China.

Wu, H.L., et al., 2019. Experimental and numerical investigation of the hydroelasticity of a floating structure with legs. Mar. Struct. 61, 100–118.

Wu, Y.S., Maeda, H., Kinoshita, T., 1997. The second order hydrodynamic actions on a flexible body. Seisan Kenkyu 49 (4), 8–13. Tokyo.

Wang Y., D., Wu S., Y., 1996. Three dimensional hydroelastic analysis in time domain with applications to an elastic ship model. J. Hydrodyn. 10 (4), 54–61.

Wu, Y.S., 1984. Hydroelasticity of Floating Bodies. Ph.D., Thesis. Brunel University, U.K.

Yang, P., 2016. 3D Nonlinear Hydro-Elastic Response Study of Ships in Time Domain (Doctoral thesis,). China Ship Scientific Research Center, Wuxi, China (In Chinese).

Yang, P., et al., 2018. 3D nonlinear hydroelastic response and load prediction of a large bulk carrier in time domain. J. Ship Mech. 22 (12), 1495–1507.